SCIENTIFIC REPORTS

OPEN

High-temperature quantum oscillations of the Hall resistance in bulk Bi_2Se_3

Received: 25 September 2017
Accepted: 19 December 2017
Published online: 11 January 2018

Marco Busch[1], Olivio Chiatti[1], Sergio Pezzini[2], Steffen Wiedmann[2], Jaime Sánchez-Barriga[3], Oliver Rader[3], Lada V. Yashina[4] & Saskia F. Fischer[1]

Helically spin-polarized Dirac fermions (HSDF) in protected topological surface states (TSS) are of high interest as a new state of quantum matter. In three-dimensional (3D) materials with TSS, electronic bulk states often mask the transport properties of HSDF. Recently, the high-field Hall resistance and low-field magnetoresistance indicate that the TSS may coexist with a layered two-dimensional electronic system (2DES). Here, we demonstrate quantum oscillations of the Hall resistance at temperatures up to 50 K in nominally undoped bulk Bi_2Se_3 with a high electron density n of about $2{\cdot}10^{19}$ cm^{-3}. From the angular and temperature dependence of the Hall resistance and the Shubnikov-de Haas oscillations we identify 3D and 2D contributions to transport. Angular resolved photoemission spectroscopy proves the existence of TSS. We present a model for Bi_2Se_3 and suggest that the coexistence of TSS and 2D layered transport stabilizes the quantum oscillations of the Hall resistance.

Among the new material class of topological insulators (TI), the chalcogenide semiconductor Bi_2Se_3 has been long subject to intense investigations due to its potential integration in room temperature applications, such as dissipationless electronics and spintronics devices[1–4]. Bi_2Se_3 has a single Dirac cone at the Γ-point in the first surface Brillouin zone and a direct band gap of 0.3 eV between the valence and the conduction band[5–7]. Due to the inversion symmetry in Bi_2Se_3 the topological Z_2 invariant $\nu = (1;000)$ is equal to the charge of parity of the valence band eigenvalues at the time-reversal-invariant points of the first Brillouin zone caused by the band inversion[8]. In the crystalline modification Bi_2Se_3 has a tetradymite structure with $R\bar{3}m$ symmetry. The unit cell consists of 15 atomic layers grouped in three quintuple layers with Se–Bi–Se–Bi–Se order stacked in an A–B–C–A–B–C manner. The quintuple layers are van der Waals bonded to each other by a double layer of Se atoms, the so-called van der Waals gap[4]. The existence of TSS in Bi_2Se_3 has been experimentally confirmed through angle resolved photoemission spectroscopy (ARPES)[3,7,9] and scanning tunneling microscopy/scanning tunneling spectroscopy (STM/STS)[10,11]. The as-grown crystals of Bi_2Se_3 are typically n-type because of electron doping due to natural selenium vacancies[12,13]. Therefore, the transport properties of Bi_2Se_3 are generally dominated by bulk conduction. In particular, the temperature dependence of the electrical resistivity ρ is metallic-like[3,14–17] and Shubnikov-de Haas (SdH) oscillations in the longitudinal resistivity ρ_{xx} show the characteristic signatures for a 3D Fermi surface[14,17]. For highly Sb-doped samples with lower carrier density $n \sim 10^{16}$ cm^{-3}, the TSS can be detected via additional SdH oscillations with a frequency B_{SdH} higher than that of the bulk and the Hall resistivity ρ_{xy} exhibits quantum oscillations for a carrier density $n < 5 \cdot 10^{18}$ cm^{-3} (ref.[18]). Different from that, for $n \geq 2 \cdot 10^{19}$ cm^{-3} a bulk quantum Hall effect (QHE) with 2D-like transport behavior was reported[3,16]. Its origin remains unidentified.

In this work we demonstrate that the quantum oscillations of the Hall resistance R_{xy} in high-purity, nominally undoped Bi_2Se_3 single crystals with a carrier density of $n \approx 2 \cdot 10^{19}$ cm^{-3} persists up to high temperatures. The quantum oscillations in R_{xy} scale with the sample thickness, strongly indicating 2D layered transport. These findings stand out because the Bi_2Se_3 samples investigated here have a lower carrier mobility μ of about 600 cm^2/(Vs) than materials hosting a typical 2D Fermi gas[19–22] or 3D Fermi gas[23–25] showing QHE. We discuss the conditions of the QHE below in detail and present a model for the coexistence of 3D bulk, 2D layered and TSS transport.

[1]Novel Materials Group, Humboldt-Universität zu Berlin, Newtonstraße 15, 12489, Berlin, Germany. [2]High Field Magnet Laboratory, Radboud University Nijmegen, P.O. Box 9010, 6500 GL, Nijmegen, Netherlands. [3]Helmholtz-Zentrum-Berlin für Materialien und Energie, Albert-Einstein-Straße 15, 12489, Berlin, Germany. [4]Department of Chemistry, Moscow State University, Leninskie Gory 1/3, 119991, Moscow, Russia. Correspondence and requests for materials should be addressed to S.F.F. (email: sfischer@physik.hu-berlin.de)

Results

Experimental data. High-resolution ARPES dispersions measured at a temperature of 12 K for two representative photon energies of $h\nu = 16$ eV and 21 eV are shown in Fig. 1a and b, respectively. We clearly observe distinct intensity contributions from the bulk conduction band (BCB) and bulk valence band (BVB) coexisting with sharp and intense Dirac cone representing the TSS. The BCB crossing the Fermi level indicates that the crystals are intrinsically *n*-type, in agreement with our Hall measurements on the same samples. At binding energies higher than the Dirac node ($E_D \sim 0.35$ eV), the lower half of the TSS overlaps with the BVB. By changing the photon energy we select the component of the electron wave vector perpendicular to the surface k_z. Since the lattice constant of Bi_2Se_3 is very large along the *z* direction ($c = 28.64$ Å), the size of the bulk Brillouin zone (BBZ) is very small (~ 0.2 Å^{-1}). With photon energies between 16 to 21 eV we cross practically the complete BBZ, enhancing the sensitivity to the out-of-plane dispersion of the bulk bands. We note that the ARPES intensity changes with the photon energy as well due to the k_z-dependence of the photoemission transitions. Differently from the BCB or BVB, the TSS exhibits no k_z-dependence due to its 2D character. Consistent with the direct nature of the gap, we find the BCB minimum ($\approx\Gamma$-point of the BBZ) at a binding energy of ~ 0.154 eV, while the BVB maximum is at ~ 0.452 eV. In particular, from the ARPES measurements, we estimate a bulk carrier density of $n_{3D,BCB} = 1.77 \cdot 10^{19}$ cm^{-3} and a sheet carrier density of $n_{2D,TSS} = k_{F,TSS}^2/(4\pi) = 1.18 \cdot 10^{13}$ cm^{-2}, with $k_{F,3D} = 0.064$ Å^{-1} and $k_{F,TSS} = (0.086 \pm 0.001)$ Å^{-1}, respectively.

In the following, we present data measured on one Bi_2Se_3 macro flake. However, similar results were obtained for other samples from the same source bulk single crystal. The longitudinal resistance R_{xx} and the Hall resistance R_{xy} were measured simultaneously in a temperature range between 0.3 K and 72 K in tilted magnetic fields up to 33 T. R_{xx} as a function of perpendicular magnetic field *B* measured at $T = 0.47$ K is shown in Fig. 1c as symmetrized raw data $R_{xx}^{sym}(B) = [R_{xx}^{raw}(+B) + R_{xx}^{raw}(-B)]/2$. The temperature-dependent R_{xx} at zero magnetic field shows metallic-like behavior (see inset of Fig. 1c). A residual resistance ratio $RRR = R_{xx}(288\text{ K})/R_{xx}(4.3\text{ K}) = 1.63$ indicates a high crystalline quality[12] (see Supplementary Information Sec. 1).

The longitudinal resistivity ρ_{xx} and the Hall resistivity ρ_{xy} as a function of the perpendicular magnetic field *B* at a temperature of $T = 0.47$ K are shown in Fig. 1d (ρ_{xx}: blue curve, left axis; ρ_{xy}: red curve, right axis). The onset of quantum oscillations with plateaux-like features in ρ_{xy} and SdH oscillations in ρ_{xx} can be observed at fields $B \geq 10$ T. The low-field slope of ρ_{xy} yields a carrier density of $n_{Hall} = 1.97 \cdot 10^{19}$ cm^{-3} and a carrier mobility of $\mu_{Hall} = 594$ cm^2/(Vs).

In order to analyze the plateaux-like features in R_{xy}, we use the high-field anti-symmetrized Hall resistance $R_{xy}^{asy}(B) = \left[R_{xy}^{raw}(+B) - R_{xy}^{raw}(-B)\right]/2$ data for $T = 0.47$ K and an angle of $\theta = 0°$. θ denotes the angle between the direction of $\vec{B}$ and the surface normal $\vec{N}$ of the Bi_2Se_3 macro flake (i. e. $\theta = 0°$ means $\vec{B} \,||\, \vec{N}$). $\vec{N}$ is parallel to the *c*-axis of the single crystal. The scaling behaviour of $\Delta R_{xy}^{asy} = R_{xy}^{asy}(N) - R_{xy}^{asy}(N+1)$ with the thickness leads to $Z^* = \left[(1/N - 1/(N+1))/\Delta R_{xy}^{asy}\right] \cdot (h/(2e^2))$ as the number of 2D spin-degenerate layers contributing to the transport. Conclusively, an average number of 2D layers of $Z^* = 25250$ is derived. The variation of Z^* for different Landau level (LL) index *N* is given in the inset of Fig. 2a.

The negative differentiated Hall resistivity $-d\rho_{xy}/dB$ vs magnetic field *B* is shown for different angles θ at constant $T = 1.47$ K in Fig. 2c, and for different temperatures *T* at constant $\theta = 0°$ in Fig. 2d. In accordance with the angular and the temperature dependence of the SdH oscillations, as shown in Figs 3a and 4a, respectively, a decreasing amplitude of the differentiated Hall resistivity with increasing θ and increasing *T* is detected. At a constant $T = 1.47$ K the typical signatures of quantum oscillations of the Hall resistance are observed up to $\theta = 61.8°$ and at $\theta = 0°$ the amplitude of $d\rho_{xy}/dB$ vanishes only for temperatures above 71.5 K.

The SdH oscillations in the longitudinal resistivity ρ_{xx} are periodic functions of the inverse magnetic field $1/B$ and the minima correspond to an integer number of filled LLs. Since the degeneracy of states in the LLs is proportional to *B*, the inverse magnetic-field positions of the ρ_{xx} minima are linear functions of the LL index. The slopes of the linear functions depend on the extremal cross-sectional area of the Fermi sphere (for 3D systems) or circle (for 2D systems), and the intercepts depend on the Berry phase of the charge carriers (see Supplementary Information Sec. 2). In the LL fan diagram shown in Fig. 2b the inverse magnetic-field positions $1/B_{\bar{n}}$ are plotted vs the $\bar{n}$th minimum of the longitudinal resistivity ρ_{xx} for different values of θ. The straight dashed lines, which represent the best linear fits to the data, intersect jointly the $\bar{n}$-axis at the point of origin (see Supplementary Information Sec. 2). Hence, we find for all angles θ and temperatures *T* investigated here a significant evidence for a trivial Berry phase of $\Phi_B = 0$ (cf. inset of Fig. 2b) and conclude the dominance of non-relativistic fermions. For an improved estimate of the Berry phase we have fitted the behavior of the relative longitudinal resistivity $\Delta\rho_{xx}$ vs magnetic field *B* assuming 2D and 3D transport (cf. Fig. 4c and d, respectively).

The relative longitudinal resistivity $\Delta\rho_{xx}$ vs magnetic field *B* measured at $T = 4.26$ K for different angles θ is shown in Fig. 3a. $\Delta\rho_{xx}$ was calculated from the measured ρ_{xx} by subtracting a suitable polynominal fit to the background to extract the oscillatory component. The amplitude of the SdH oscillations decreases with increasing angle θ, and is really marginal for $\theta > 70°$. Furthermore, a change in the frequency of the SdH oscillations with increasing angle θ with respect to $\theta = 0°$ is observed. For all values of θ and *T*, we found one value of the SdH frequency B_{SdH}, deduced from the periodicity in the $1/B$ dependence. These values are in agreement with those determined from the slopes of the lines in the LL fan diagram (Fig. 2b) and from fast Fourier transforms of the same data. The absence of additional frequencies and beatings, as well as the angular dependence of B_{SdH} (see Fig. 3b), are significant evidence of a single 3D (non-spherical) Fermi surface (see Supplementary Information Sec. 3).

The temperature dependence of $\Delta\rho_{xx}$ is shown in Fig. 4a: the amplitude decreases with increasing temperature *T*, and oscillations are not observed for $T > 71.5$ K. From the fitting of the relative longitudinal resistivity ratio $\Delta\rho_{xx}(T)/\Delta\rho_{xx}(T = 1.47\text{ K})$, we deduce an effective mass of the charge carriers of $m^* \cong 0.16\, m_e$ ($m_e = 9.10938356 \cdot 10^{-31}$ kg denotes the electron rest mass) and a Fermi velocity of $v_F = \hbar k_{F,3D}/m^* = 0.46 \cdot 10^6$ m/s, with $k_{F,3D} = 0.064$ Å^{-1}.

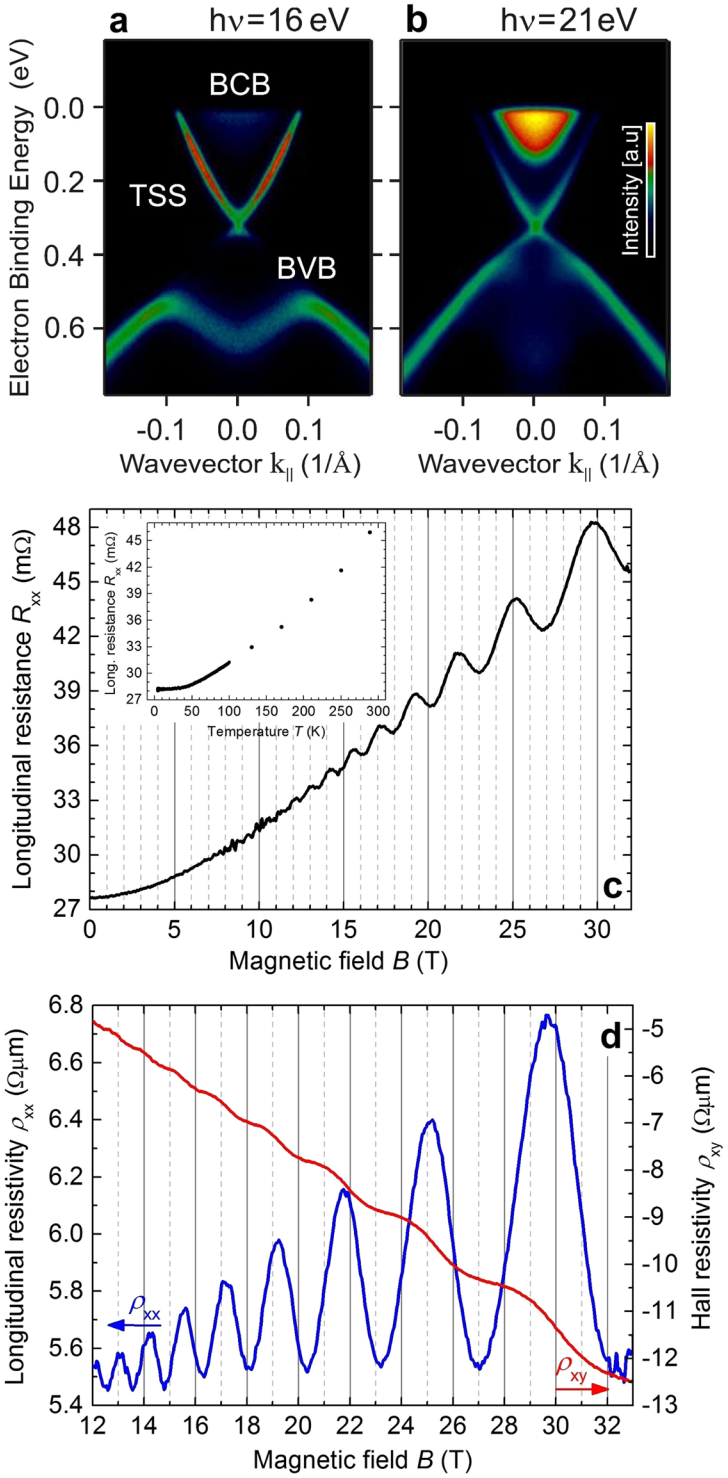

Figure 1. Electronic structure, temperature-dependent resistance and magnetotransport properties of Bi_2Se_3. (**a**) and (**b**) Electronic structure of the Bi_2Se_3 bulk single crystal before mechanical exfoliation. The panels show high resolution ARPES $E(k_{||})$ dispersions measured at a temperature of $T = 12$ K and at a photon energy of $h\nu = 16$ eV and 21 eV, respectively. In (**a**), the TSS, the bulk conduction band (BCB) and the bulk valence band (BVB) are indicated. (**c**) Longitudinal resistance R_{xx} vs perpendicular magnetic field B as symmetrized raw data measured at $T = 0.47$ K. Inset: Longitudinal resistance R_{xx} vs temperature T measured for $B = 0$. (**d**) Longitudinal resistivity ρ_{xx} (blue curve, left axis) and Hall resistivity ρ_{xy} (red curve, right axis) vs perpendicular magnetic field B measured at $T = 0.47$ K.

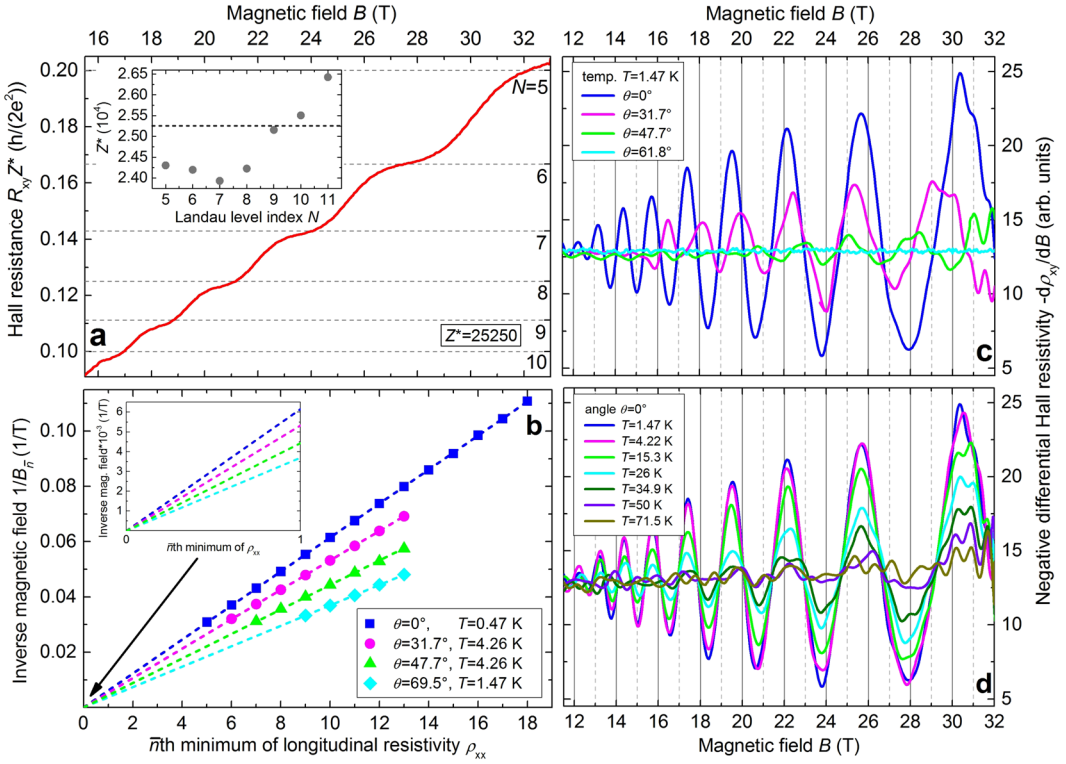

Figure 2. Quantum oscillations of the Hall resistance. (**a**) Hall resistance $\widetilde{R}_{xy} = R_{xy}Z^*$ in units of $h/(2e^2)$ with an averaged number of 2D layers $Z^* = 25250$ vs magnetic field B at $T = 0.47$ K and $\theta = 0°$. Inset: Number of 2D layers Z^* vs Landau level (LL) index N. The averaged number of 2D layers $Z^* = 25250$ is shown as dashed line. (**b**) LL fan diagram from SdH oscillations of longitudinal resistivity ρ_{xx} for different values of the angle θ between the direction of the magnetic field $\vec{B}$ and the surface normal $\vec{N}$ of the Bi_2Se_3 macro flake and for different temperatures T. The dashed lines represent the best linear fits to the data. Inset: Enlargement of the LL fan diagram for $0 \leq \bar{n} \leq 1$. (**c**) and (**d**) Negative differential Hall resistivity $-d\rho_{xy}/dB$ vs magnetic field B, for different values of the angle θ at $T = 1.47$ K and at different temperatures T for $\theta = 0°$, respectively.

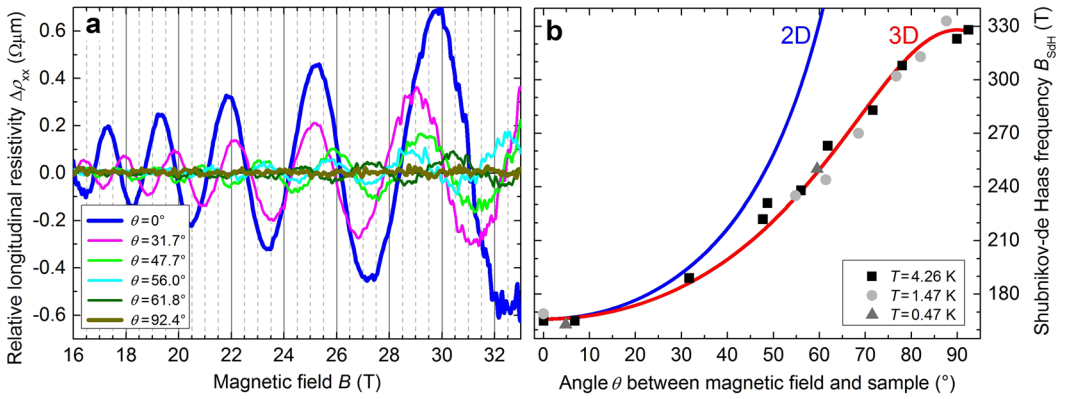

Figure 3. Angular-dependence of Shubnikov-de Haas oscillations. (**a**) Relative longitudinal resistivity $\Delta\rho_{xx}$ vs magnetic field B measured at $T = 4.26$ K for different values of the angle θ. (**b**) SdH frequency B_{SdH} vs angle θ determined at temperatures $T = 0.47$ K (dark gray triangles), 1.5 K (light gray circles), and 4.26 K (black squares). Curves represent calculated behavior for a planar 2D Fermi surface assuming $B_{SdH}^{2D} = B_{\perp}/\cos\theta$ (blue curve) and for an ellipsoidal 3D Fermi surface assuming $B_{SdH}^{3D} = B_{\perp}B_{||}/\sqrt{(B_{\perp}\cos\theta)^2 + (B_{||}\sin\theta)^2}$ (red curve) with $B_{\perp} = 166$ T (for $\theta = 0°$) and $B_{||} = 328$ T (for $\theta = 90°$).

In a first step we assumed 2D transport in accordance with some other investigations[14,15,26]. The Dingle plots (inset of Fig. 4b) at temperatures of $T = 1.47$ K, 4.22 K, 15.3 K, and 26 K yield the following Dingle scattering time (also known as single-particle relaxation time) τ_D and the Dingle temperature $T_D = h/(4\pi^2 k_B \tau_D)$, assuming the fit function $-\pi m^*/(e\tau_D B)$ with $m^* = 0.16\, m_e$: $\tau_D = 5.8 \cdot 10^{-14}$ s ($T_D = 20.8$ K), $5.1 \cdot 10^{-14}$ s (23.7 K), $3.9 \cdot 10^{-14}$

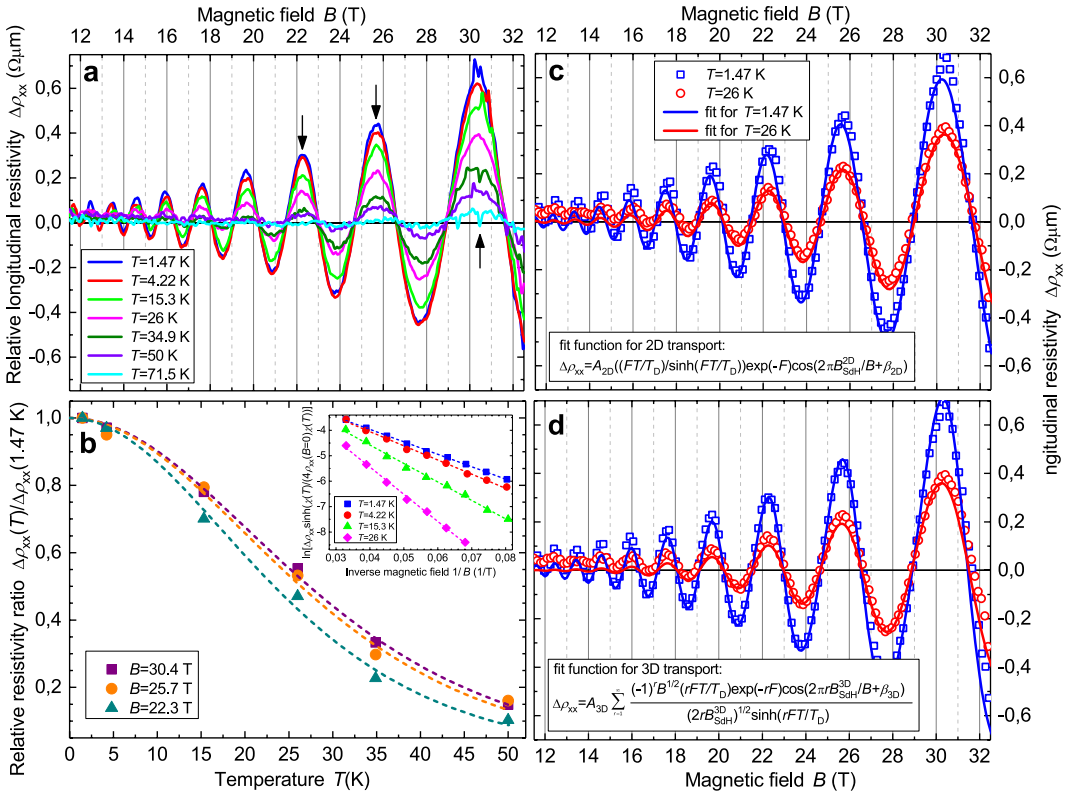

Figure 4. 2D and 3D analysis of the temperature dependence of the Shubnikov-de Haas oscillations. (**a**) Relative longitudinal resistivity $\Delta\rho_{xx}$ vs magnetic field B measured for an angle $\theta = 0°$ at different temperatures T. The black arrows indicate values of magnetic field B shown in panel b vs temperature T. (**b**) Relative longitudinal resistivity ratio $\Delta\rho_{xx}(T)/\Delta\rho_{xx}(1.47\ \mathrm{K})$ vs temperature T for a magnetic field of $B = 30.4$ T (violet squares), 25.7 T (orange circles), and 22.3 T (dark cyan triangles). Dashed curves represent best fits to data assuming the function $\chi(T)/\sinh(\chi(T))$, with $\chi(T) = (4\pi^3 m^* k_B T)/(heB)$. Inset: Dingle plots of the SdH oscillations with 2D transport (maxima of relative longitudinal resistivity $\Delta\rho_{xx}$ as shown in panel (a)) at $T =$ 1.47 K (blue squares), 4.22 K (pink circles), 15.3 K (green triangles), and 26 K (cyan diamonds). Dashed lines represent best linear fits to data with the function $-\pi m^*/(e\tau_D B)$, with $m^* = 0.16\, m_e$. (**c**) Relative longitudinal resistivity $\Delta\rho_{xx}$ vs magnetic field measured for $\theta = 0°$ at $T = 1.47$ K (blue squares) and 26 K (pink circles). For clarity, only every fifth data point is shown. The curves are best fits to the Lifshitz-Kosevich formula for 2D transport (given in the legend), with $B^{2D}_{SdH} = 166$ T (cf. Fig. 3b and text). (**d**) Same data as in (**c**): The curves are best fits to the Lifshitz-Kosevich formula for 3D transport (given in the legend), with $B^{3D}_{SdH} = 169.5$ T and the parameter $F = 2\pi\, k_B T_D/(\hbar\omega_C) = m^*/(\tau_D eB)$ and $m^* = 0.16\, m_e$. The parameter r denotes the number of harmonic oscillations. In the present study we considered a range of values of $1 \le r \le 20$.

s (30.9 K) and $2.7 \cdot 10^{-14}$ s (45.5 K), respectively. For a more detailed analysis we have fitted the magnetic-field dependence of $\Delta\rho_{xx}$ (see Supplementary Information Sec. 4) and have used as fit function the Lifshitz-Kosevich formula[4,27,28] for 2D transport. We found a reasonably good agreement between experimental data and the calculated behavior for $\Delta\rho_{xx}(B)$ (cf. Fig. 4c).

However, in a second step we also performed fits under the assumption of 3D transport[29] (cf. Fig. 4d), because the angular dependence of the SdH frequency B_{SdH} in Fig. 3b clearly follows the function for 3D transport. In this case, we find for all curves a single value for the Dingle temperature $T_D = 23.5$ K and hence a single value for the Dingle scattering time $\tau_D = 5.2 \cdot 10^{-14}$ s, consistent with a nearly constant $R_{xx}(T)$ up to $T = 30$ K (see inset of Fig. 1c). From τ_D and the effective mass $m^* = 0.16\, m_e$, we determined a carrier mobility of $\mu_D = e\tau_D/m^* = 572$ cm^2/(Vs).

Evaluation of experimental data. Most of the investigations of bulk Bi_2Se_3 conclude that the Fermi surface is 3D[3,12,14,17,30], usually from the angular dependence of the SdH oscillations. However, in the search of TSS and QHE some works evaluated the Fermi surface as 2D[15,16]. Our analysis of the SdH oscillations (see above) indicates that the Fermi surface is 3D. This is confirmed by our following analysis of the angular dependence of the SdH frequencies.

The angle dependence of the SdH oscillations determines that the Fermi surface has an ellipsoidal shape. For a plane 2D Fermi surface, the SdH oscillation frequency is equal to $B^{2D}_{SdH}(\theta) = B_\perp / \cos\theta$, with $B^{2D}_{SdH}(\theta) \to \infty$ for $\theta \to 90°$ (blue curve in Fig. 3b), and for an ellipsoidal 3D Fermi surface it is $B^{3D}_{SdH}(\theta)) = B_\perp B_{||}/\sqrt{(B_{||}\cos\theta)^2 + (B_\perp \sin\theta)^2}$ (red curve in Fig. 3b), with $B_\perp = B^{3D}_{SdH}(\theta = 0°) = B^{2D}_{SdH}(\theta = 0°) = 166$

T and $B_{||} = B^{3D}_{SdH}(\theta = 90°) = 328$ T. Previous data[15,16] may also be interpreted as 3D ellipsoidal Fermi surface (see Supplementary Information Sec. 3).

We estimate the ellipsoidal cross-section of the 3D Fermi surface with the wave vectors $k^{(a)}_{F,SdH} = k^{(b)}_{F,SdH} = \sqrt{2eB_{\perp}/\hbar} = 0.071$ Å^{-1} and $k^{(c)}_{F,SdH} = 2eB_{||}/(\hbar k^{(a)}_{F,SdH}) = 0.14$ Å^{-1}. With these values we deduced an eccentricity for the 3D non-spherical Fermi surface of $k^{(c)}_{F,SdH}/k^{(a)}_{F,SdH} = 1.98$. Köhler[30] and Hyde *et al.*[12] show, that the eccentricity of the Fermi surface decreases with decreasing carrier density n. In accordance with the present study, Eto *et al.*[14] deduced for a Bi_2Se_3 bulk single crystal with a lower carrier density of $n = 3.4 \cdot 10^{18}$ cm^{-3} an eccentricity of $k^{(c)}_{F,SdH}/k^{(a)}_{F,SdH} = 1.62$, consistent with eccentricities obtained by Köhler[30]. Assuming a parabolic dispersion and using the values of $k^{(a)}_F$ and $k^{(c)}_F$ from the SdH analysis and of E_F from the ARPES measurements, we estimate with $E_F = (\hbar k_F)^2/(2\,m^*)$ for the effective masses $m^*_a = m^*_b = 0.125\,m_e$ and $m^*_c = 0.485\,m_e$. An average value for the effective mass is then given by[31] $1/m^* = (1/m^*_c + 2/m^*_a)/3$, which yields $m^* = 0.166\,m_e$. This value is consistent with the value obtained from the temperature dependence of the SdH oscillations: $m^*_{SdH} = 0.16 m_e$.

Discussion

Generally, a bulk or 3D QHE is attributed to parallel 2D conduction channels, each made from one or a few stacking layers. A bulk QHE, where quantized values of the Hall resistance R_{xy} inversely scale with the sample thickness, has been observed in a number of anisotropic, layered electronic bulk materials, e.g., GaAs/AlGaAs multi-quantum wells[20], Bechgaard salts[24,32] and also in Fe-doped Bi_2Se_3 bulk samples[33], where transport by TSS was excluded. However, the observation of the quantum oscillations of the Hall resistance in Bi_2Se_3 at elevated temperatures calls for a special condition considering the usual requirement of $\mu B \gg 1$. In the present case $B_{max} = 33$ T and the carrier mobility $\mu \approx 600$ cm^2/(Vs) yields only $\mu B_{max} \approx 2$. Furthermore, the deduced effective mass $m^* = 0.16\,m_e$ yields for a magnetic field of $B = 10$ T, where we observe the onset of the quantum oscillations, a value for the LL energy splitting of $\hbar\omega_c = \hbar eB/m^* \approx 7$ meV. However, the thermal energy amounts to $k_BT \approx 4$ meV at $T = 50$ K, while $\hbar\omega_c \gg k_BT$ is usually required for a QHE. Nevertheless, we observe unambiguous quantum oscillations in $-d\rho_{xy}/dB$ (Fig. 2c and d) as signature of a QHE.

In order to explain the experimental observations, we propose the following model. The Bi_2Se_3 bulk sample investigated here may consist of three different conducting regions: a semiconducting-like core region, surrounded by a metallic-like shell region and the topological surface (see Fig. S1 in Supplementary Information Sec. 5). The semiconducting-like core was proven by the preparation of semiconducting micro flakes[3]. The metallic-like shell region due to Se depletion dominates the transport mechanism observed here as metallic and 2D layered effects. From our experiments, we assume the shell to form a stacked system of 2D layers with a periodic potential[23] either due to the van der Waals-gaps or the unit cell along the c-axis because of the carrier density modulation due to Se vacancies. In magnetic fields $B \neq 0$ the thickness scaling of the plateaux-like features in the Hall resistance yields an effective thickness for the shell of stacked 2D layers. For the charge carrier density, we estimate three different values for the core (from ref.[3]), the shell (from the Hall measurements) and the topological surface (from the ARPES measurements): $n_{core} \approx 1.2 \cdot 10^{17}$ cm^{-3}, $n_{shell} \approx 2 \cdot 10^{19}$ cm^{-3} and $n_{TSS} = 1.2 \cdot 10^{13}$ cm^{-2}, respectively. In the semiconducting-like core region, the Fermi level (chemical potential) is in the gap close to the bottom of the conduction band, whereas in the metallic-like shell region the Fermi level is in the conduction band (see Supplementary Information Sec. 5). Because of a finite scattering rate between the 2D layers in the shell region $\rho_{xx}(B)$ shows considerable 3D character in the SdH oscillations for higher angles θ, and the quantization in $\rho_{xy}(B)$ even at the lowest temperature T is not exact and the plateaux have a finite slope.

For the SdH frequency B_{SdH} we estimate at $\theta = 0°$ for the three regions the following values: $B_{SdH,core} = 4.82$ T, $B_{SdH,shell} = 166$ T and $B_{SdH,TSS} = 248$ T. The small value $B_{SdH,core}$ corresponds to a slow-changing background which is out of the measurement range of our experimental setup. The larger value of the TSS is caused only by the small number of surface electrons with respect to the large number of bulk electrons ($N_{bulk} \approx N_{shell} \approx 2 \cdot 10^{15}$ and $N_{TSS} \approx 3 \cdot 10^{11}$ yield a ratio $N_{TSS}/N_{bulk} \approx 10^{-4}$). Therefore, from the experimental data we deduce only the B_{SdH} value for the shell (see Fig. 3a) and find the dominant contribution of the bulk (core + shell) in the transport behavior. A periodic modulation of the charge carrier density along the c-direction would result in a miniband structure for the LLs and, as long as the Fermi level is in a gap between these minibands, the Hall resistivity ρ_{xy} will be quantized and scale with the periodicity of the potential[23].

According to our estimate of the width of the LLs (see above), the persistence of the quantum oscillations in the Hall resistance up to high temperatures requires a special condition: We propose a Fermi level pinning in the miniband gap, which could be the result of an interaction with the existing TSS. Theoretically, due to the inter-layer coupling, it is expected that in the quantum Hall state the edge states of the stacked 2D layers form a sheath at the surface[34]. Due to the finite width of the wave functions at the surface, this sheath can interact with the TSS. This opens the possibility that the TSS act as electron reservoirs to pin the Fermi level in a miniband gap as the magnetic field is varied over a finite range. Therefore, we conclude that the observation of the quantum oscillations of the Hall resistance at higher temperatures in Bi_2Se_3 ($n \approx 2 \cdot 10^{19}$ cm^{-3}) with a majority of non-Dirac fermions is related to the existence of the TSS. Based on our results, we propose that other 3D materials with TSS and a periodic potential modulation may show quantization effects in the Hall resistance at elevated temperatures.

Methods

High-quality single crystalline Bi_2Se_3 was prepared from melt with the Bridgman technique. The growth time, including cooling was about 2 weeks for a ~50 g crystal. The whole crystal was easily cleaved along the [00.1] growth direction, indicating crystal perfection. The macro flake was prepared by cleaving the bulk single crystal with a thickness of around 110 μm to investigate bulk properties.

We explored the structural properties of the bulk single crystal[3] with atomic force microscopy (AFM), scanning transmission electron microscopy (STEM) and high-resolution transmission electron microscopy (HRTEM). The composition and surface stability were investigated using energy-dispersive x-ray spectroscopy (EDX) and spatially resolved core-level X-ray PEEM. Structural analysis using HRTEM and STEM was carried out at a JEOL JEM2200FS microscope operated at 200 kV. The sample preparation for HRTEM characterization consisted of ultrasonic separation of the flakes from the substrate, followed by their transfer onto a carbon-coated copper grid. Using adhesive tape, the surface was prepared by cleavage of the crystal along its trigonal axis in the direction perpendicular to the van-der-Waals-type (0001) planes. The ARPES measurements were performed at a temperature of 12 K in an ultra-high vacuum (UHV) chamber at a pressure of $\sim 5 \cdot 10^{-10}$ mbar with a VG Scienta R8000 electron analyzer at the UE112-PGM2a beamline of BESSY II using p-polarized undulator radiation.

Magnetotransport experiments were performed using standard low-noise lock-in techniques (Stanford Research Systems SR830 with a Keithley 6221 as current source), with low excitation to prevent heating of the sample. The Bi_2Se_3 macro flake was mounted in a flow cryostat (1.3 K to 300 K), as well as in a ^{3}He insert (down to 0.3 K), in a Bitter magnet with a bore diameter of 32 mm and magnetic fields up to 33 T at the High Field Magnet Laboratory of the Radboud University Nijmegen. In both setups, a Cernox thermometer in the vicinity of the sample was used to monitor the temperature *in situ*. In the ^{3}He system, the temperature between 0.3 K and 1.3 K was stabilized by the ^{3}He vapour pressure prior to the magnetic field sweep to assure a constant temperature. However, the temperature between 1.3 K and 4.2 K was stabilized by the ^{4}He pressure. Above a temperature of 4.2 K, we have used the flow cryostat and stabilized the temperature using a capacitance.

References

1. Xue, Q.-K. Nanoelectronics: A topological twist for transistors. *Nature Nanotechnol.* **6**, 197 (2011).
2. Zhang, H. *et al*. Topological insulators in Bi_2Se_3, Bi_2Te_3 and Sb_2Te_3 with a single Dirac cone on the surface. *Nature Phys.* **5**, 438 (2009).
3. Chiatti, O. *et al*. 2D layered transport properties from topological insulator Bi_2Se_3 single crystals and micro flakes. *Sci. Rep.* **6**, 27483 (2016).
4. Ando, Y. Topological InsulatorMaterials. *J. Phys. Soc. J.* **82**, 102001 (2013).
5. Checkelsky, J. G., Hor, Y. S., Cava, R. J. & Ong, N. P. Bulk band gap and surface state conduction observed in voltage-tuned crystals of the topological insulator Bi_2Se_3. *Phys. Rev. Lett.* **106**, 196801 (2011).
6. Betancourt, J. *et al*. Complex band structure of topological insulator Bi_2Se_3. *J. Phys.: Condens. Matter* **28**, 395501 (2016).
7. Xia, Y. *et al*. Observation of a large-gap topological-insulator class with a single Dirac cone on the surface. *Nature Phys.* **5**, 398 (2009).
8. Fu, L. & Kane, C. L. Topological insulators with inversion symmetry. *Phys. Rev. B* **76**, 045302 (2007).
9. Bianchi, M. *et al*. The electronic structure of clean and adsorbate-covered Bi_2Se_3: an angle-resolved photoemission study. *Semicond. Sci. Technol.* **27**, 124001 (2012).
10. Alpichshev, Z. *et al*. STM Imaging of Impurity Resonances on Bi_2Se_3. *Phys. Rev. Lett.* **108**, 206402 (2012).
11. Liu, Y. *et al*. Tuning Dirac states by strain in the topological insulator Bi_2Se_3. *Nature Phys.* **10**, 294 (2014).
12. Hyde, G. R., Beale, H. A., Spain, I. L. & Woollam, J. A. Electronic properties of Bi_2Se_3 crystals. *J. Phys. Chem. Solids* **35**, 1719 (1974).
13. Yan, B., Zhang, D. & Felser, C. Topological surface states of Bi_2Se_3 coexisting with Se vacancies. *Phys. Status Solidi RRL* **7**, 148 (2013).
14. Eto, K., Ren, Z., Taskin, A. A., Segawa, K. & Ando, Y. Angular-dependent oscillations of the magnetoresistance in Bi_2Se_3 due to the three-dimensional bulk Fermi surface. *Phys. Rev. B* **81**, 195309 (2010).
15. Petrushevsky, M. *et al*. Probing the surface states in Bi_2Se_3 using the Shubnikov-de Haas effect. *Phys. Rev. B* **86**, 045131 (2012).
16. Cao, H. *et al*. Quantized Hall Effect and Shubnikov-de Haas Oscillations in Highly Doped Bi_2Se_3: Evidence for Layered Transport of Bulk Carriers. *Phys. Rev. Lett.* **108**, 216803 (2012).
17. Analytis, J. G. *et al*. Bulk Fermi surface coexistence with Dirac surface state in Bi_2Se_3: A comparison of photoemission and Shubnikov-de Haas measurements. *Phys. Rev. B* **81**, 205407 (2010).
18. Analytis, J. G. *et al*. Two-dimensional surface state in the quantum limit of a topological insulator. *Nature Phys.* **6**, 960 (2010).
19. Beenakker, C. W. J. & van Houten, H. Quantum transport in semiconductor nanostructures. *Sol. St. Phys.* **44**, 1 (1991).
20. Störmer, H. L., Eisenstein, J. P., Gossard, A. C., Wiegmann, W. & Baldwin, K. Quantization of the Hall effect in an anisotropic three-dimensional electronic system. *Phys. Rev. Lett.* **56**, 85 (1986).
21. Novoselov, K. S. *et al*. Room-Temperature Quantum Hall Effect in Graphene. *Science* **315**, 1379 (2007).
22. Khouri, T. *et al*. High-temperature quantum Hall effect in finite gapped HgTe quantum wells. *Phys. Rev. B* **93**, 125308 (2016).
23. Halperin, B. I. Possible States for a Three-Dimensional Electron Gas in a Strong Magnetic Field. *Jap. J. Appl. Phys.* **26**, 1913 (1987).
24. Hannahs, S. T., Brooks, J. S., Kang, W., Chiang, L. Y. & Chaikin, P. M. Quantum Hall effect in a bulk crystal. *Phys. Rev. Lett.* **63**, 1988 (1989).
25. Hill, S. *et al*. Bulk quantum Hall effect in η-Mo_4O_{11}. *Phys. Rev. B* **58**, 10778 (1998).
26. Yan, Y. *et al*. High-Mobility Bi_2Se_3 Nanoplates Manifesting Quantum Oscillations of Surface States in the Sidewalls. *Sci. Rep.* **4**, 3817 (2014).
27. Lifshitz, E. M. & Pitaevskii, L. P. *Statistical Physics*. (Pergamon Press, Oxford, 1986).
28. Taskin, A. A. & Ando, Y. Berry phase of nonideal Dirac fermions in topological insulators. *Phys. Rev. B* **84**, 035301 (2011).
29. Ridley, B. K. *Quantum Processes in Semiconductors*. (Oxford University Press, Oxford, 2013).
30. Köhler, H. Conduction Band Parameters of Bi_2Se_3 from Shubnikov-de Haas Investigations. *Phys. Stat. Sol. (b)* **58**, 91 (1973).
31. Ziman, J. M. *Electrons and Phonons–The Theory of Transport Phenomena in Solids*. (Clarendon Press, Oxford, 2001).
32. Balicas, L., Kriza, G. & Williams, F. I. B. Sign Reversal of the Quantum Hall Number in $(TMTSF)_2PF_6$. *Phys. Rev. Lett.* **75**, 2000 (1995).
33. Ge, J. *et al*. Evidence of layered transport of bulk carriers in Fe-doped Bi_2Se_3 topological insulators. *Sol. State Commun.* **211**, 29 (2015).
34. Balents, L. & Fisher, M. P. Chiral Surface States in the Bulk Quantum Hall Effect. *Phys. Rev. Lett.* **76**, 2782 (1996).

Acknowledgements

Financial support from the Deutsche Forschungsgemeinschaft within the priority program SPP1666 (Grant No. FI932/7-1, FI932/7-2 and RA1041/7-1) and the Bundesministerium für Bildung und Forschung (Grant No. 05K10WMA) is gratefully acknowledged.

Author Contributions

M.B., O.C., S.P., S.W. and S.F.F. contributed to the transport experiments, analyzed the data and wrote the manuscript, J.S.-B. and O.R. conducted the ARPES experiments and L.V.Y. conducted the bulk crystal growth. All authors contributed to the discussion and reviewed the manuscript.

Additional Information

Supplementary information accompanies this paper at https://doi.org/10.1038/s41598-017-18960-0.

Competing Interests: The authors declare that they have no competing interests.

Publisher's note: Springer Nature remains neutral with regard to jurisdictional claims in published maps and institutional affiliations.